Identification and Control of a Cryogenic Current Comparator Using Robust Control Theory

Marcos Eduardo Bierzychudek, Ricardo S. Sánchez-Peña, *Senior Member, IEEE*, and Alejandra Tonina

***Abstract*— This paper presents the model identification of a cryogenic current comparator (CCC). A dynamic model set is obtained and compared with the experimental data in order to provide a realistic dynamical behavior of the system. To improve the performance of the CCC, an $\mathcal{H}_\infty$ optimal controller is designed based on this model set. In this framework, a robust stability guarantee is provided and the simulations of the closed-loop system illustrate the performance and robustness improvements.**

***Index Terms*— Current comparator, $\mathcal{H}_\infty$ control, metrology, resistance measurement, superconducting quantum interference device (SQUID).**

AQ:1

Nomenclature

C_1	Primary winding capacitance (F).
L_1	Primary winding inductance (H).
R_{W_1}	Primary winding resistance (Ω).
M_{1i}	Mutual inductance between the primary winding and the winding i (H).
R_i	Resistor connected to the i winding (Ω).
N_i	Number of turns of winding i.
p	SQUID cut-off radial frequency (rad/s).
k_{SQ}	SQUID flux sensitivity (V/Φ_0).
G_{CCC}	CCC amplification (Φ_0/AT).
s	Laplace variable.
$j\omega$	Complex frequency variable.
$I_i(s)$	Equivalent current source i (A).
$I_{L_1}(s)$	Current in the primary winding (A).
$T_{L_1 i}(s)$	Transfer function from $I_i(s) \rightarrow I_{L_1}(s)$ (A/A).
$T_{\text{SQ}}(s)$	SQUID transfer function (V/Φ_0).
$G_0(s)$	Nominal model from $I_F(s) \rightarrow V_{\text{SQ}}(s)$ (Ω).
$G(s)$	Model included in set Ψ (Ω).
$K(s)$	Controller transfer function (Ω^{-1}).
$W_\Delta(s)$	Dynamic uncertainty weight.
$V(s)$	Voltage source (V).
$V_{\text{SQ}}(s)$	Laplace transform of SQUID output (V).
Δ	Dynamic uncertainty.
Ψ	Set of models.
$\mathcal{T}$	Set of closed-loop models.
$v_{\text{SQ}}(t)$	SQUID output (V).
$\hat{v}_{\text{SQ}}(t_q)$	Estimated SQUID output at time t_q (V).
$\bar{v}_{\text{SQ}}$	Mean value of SQUID output (V).
t	Continuum time variable (s).
T_s	Sampling period (s).
t_q	Sampling time (s).
q	Discrete time variable.
F_I	Fit index.

Manuscript received January 19, 2015; revised May 28, 2015; accepted June 14, 2015. The Associate Editor coordinating the review process was Dr. Branislav Djokic.

AQ:2

M. E. Bierzychudek is with the Centro de Física y Metrología, Instituto Nacional de Tecnología Industrial, Buenos Aires 8000, Argentina, and also with the Instituto Tecnológico de Buenos Aires, Buenos Aires C1106ACD, Argentina (e-mail: marcosb@inti.gob.ar).

R. S. Sánchez-Peña is with the National Scientific and Technical Research Council, Buenos Aires C1428ADN, Argentina, and also with the Instituto Tecnológico de Buenos Aires, Buenos Aires C1106ACD, Argentina (e-mail: rsanchez@itba.edu.ar).

A. Tonina is with the Centro de Física y Metrología, Instituto Nacional de Tecnología Industrial, Buenos Aires 8000, Argentina (e-mail: atonina@inti.gob.ar).

Color versions of one or more of the figures in this paper are available online at http://ieeexplore.ieee.org.

Digital Object Identifier 10.1109/TIM.2015.2459472

I. Introduction

THE outstanding sensitivity and accuracy of a cryogenic current comparator (CCC) are mainly based on its superconducting inner shield and on the superconducting quantum interference device (SQUID). The shield provides negligible ratio errors, and the sensor can detect fractions of the magnetic flux quantum [1]. However, the SQUID has nonlinear dynamics and a limited slew rate. Hence, high frequency signals and noise can affect its performance or even impede the measurements. Therefore, a common guiding principle is to design the electronics, cables, and screens, with a focus on the best SQUID performance.

This paper follows the same approach by applying robust control theory to the problem. The aim is to find a controller that improves the SQUID performance and allows faster current reversals. To this end, the feedback bandwidth must be equal to the working frequency range [2] in order to attenuate high-frequency signals at the sensor input, including distortion created on current reversal. Traditional integral control is limited by the CCC self-resonant frequency [3], as Fig. 1 shows for a two-terminal CCC [4], thus a different control framework has to be applied.

Bierzychudek *et al.* [5] developed a theoretical model of a CCC and a $\mathcal{H}_\infty$ controller design. In this paper, the model is adjusted using an identification procedure and validated by the experimental data. The first step of this process is to obtain the parameters of the model, for example, inductance and resistance, from data and/or specifications. Next, the initial model is adjusted with respect to several frequency responses of the system measured with a lock-in amplifier in order to improve its fitting. A wider hypothesis is to represent the system by a *set* of models, instead of a single model, which considers a

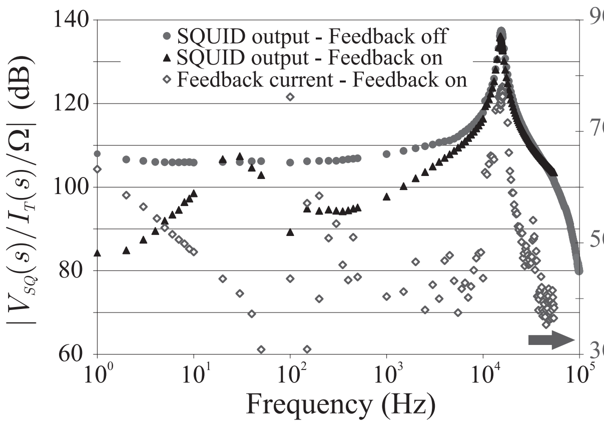

AQ:3 Fig. 1. Absolute value of the frequency response measurements of the SQUID voltage from a test current $I_T(s)$ in a single-turn winding, with integral feedback OFF (red circle) and ON (black triangle). The response of the feedback current from the same input in closed loop is shown in the secondary axis (blue diamond).

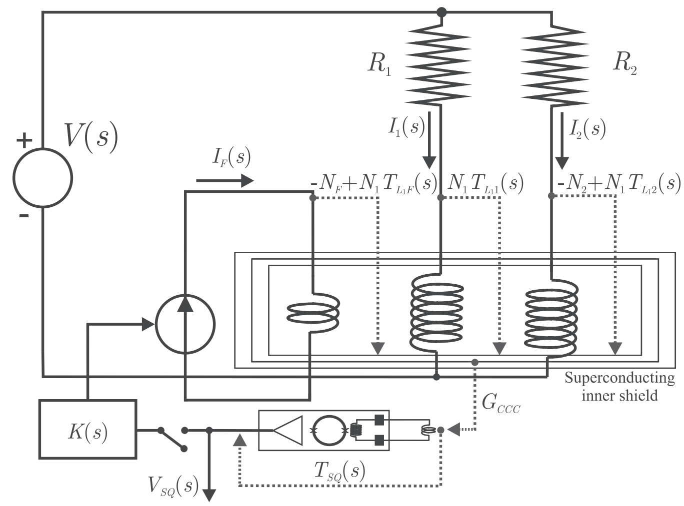

Fig. 2. Schematic of the two-terminal CCC. The notation for the transfer functions from the origin to the end of the blue-dotted arrows is indicated. In the feedback loop, a switch is included to indicate where the loop is opened.

frequency-dependent uncertainty bound. Here, the model set is compared and validated with the measurements recorded by a digital oscilloscope. Then a controller is designed based on this dynamic set of models.

The CCC under study was designed to measure two-terminal high-value resistors, scaling from the quantum Hall resistor or a 10 kΩ standard up to 1 GΩ [4], [6]. It has a single voltage source which allows a simple design and a unique ground reference, with no need of a voltage detector. In addition phosphor-bronze windings are used in order to damp the CCC resonance.

II. Background: Theoretical Model

In [5], a theoretical model of a two-terminal CCC was obtained from its electrical equivalent circuit. The dynamics of each part of the system were represented as the Laplace transform of an ordinary differential equation, i.e., a transfer function that depends on the Laplace variable s. As shown in Fig. 2, $T_{L_11}(s)$, $T_{L_12}(s)$, and $T_{L_1F}(s)$ represent the transfer functions from currents $I_1(s)$, $I_2(s)$, and $I_F(s)$ to the current in the primary winding $I_{L_1}(s)$, so $T_{L_1i}(s) = I_{L_1}(s)/I_i(s)$ with $i = 1,\ 2,\ F$. This winding has the larger number of turns and the lower resonant frequency, according to the assumption stated in [5]. These dynamics were obtained by applying the superposition principle, and considering parasitic capacitance and resistance

$$T_{L_11}(s) = \frac{1}{C_1L_1s^2 + s\left(\frac{L_1}{R_1} + C_1R_{W1}\right) + \left(\frac{R_{W1}}{R_1} + 1\right)} \tag{1}$$

$$T_{L_12}(s) = \frac{M_{12}s\left(C_1s + \frac{1}{R_1}\right)}{C_1L_1s^2 + s\left(\frac{L_1}{R_1} + C_1R_{W1}\right) + \left(\frac{R_{W1}}{R_1} + 1\right)} \tag{2}$$

$$T_{L_1F}(s) = \frac{M_{1F}s\left(C_1s + \frac{1}{R_1}\right)}{C_1L_1s^2 + s\left(\frac{L_1}{R_1} + C_1R_{W1}\right) + \left(\frac{R_{W1}}{R_1} + 1\right)}. \tag{3}$$

The resistance R_1 is the standard resistor connected to the primary winding. L_1, C_1, and R_{W_1} are the inductance, stray capacitance, and distributed resistance of the primary winding, respectively. M_{12} and M_{1F} are the mutual inductances between the primary winding, and the secondary and feedback windings, respectively. The SQUID sensor in flux locked loop (FLL) mode is represented with a single pole transfer function, $T_{\mathrm{SQ}}(s) = k_{\mathrm{SQ}}/(1 + s/p)$, which has a dc gain k_{SQ} equal to the SQUID flux sensitivity. The SQUID output voltage (4) can be obtained by applying Ampere's law to the CCC. Here, N_1, N_2, and N_F are the number of turns of the primary, secondary, and feedback windings, respectively, and G_{CCC} is the inverse of the linkage current

$$\begin{aligned} V_{\mathrm{SQ}}(s) = {}& T_{\mathrm{SQ}}(s)\ G_{\mathrm{CCC}} \\ & \cdot [I_1(s)\ T_{L_11}(s)\ N_1 - I_2(s)\ (N_2 - T_{L_12}(s)\ N_1) \\ & - I_F(s)\ (N_F - T_{L_1F}(s)\ N_1)]. \end{aligned} \tag{4}$$

The controller $K(s)$ measures the SQUID voltage and drives the feedback current (see Fig. 2). Therefore, currents $I_1(s)$ and $I_2(s)$ are outside the control loop. As a consequence, the terms $T_{L_11}(s)N_1$ and $[N_2 - T_{L_12}(s)N_1]$ do not have an effect on the closed-loop stability. Hence, this approach focuses on the transfer function from $I_F(s)$ to $V_{\mathrm{SQ}}(s)$. Using the nominal values of the parameters, the model is defined as follows:

$$G_0(s) = \frac{V_{\mathrm{SQ}}(s)}{I_F(s)} = -T_{\mathrm{SQ}}(s)\ G_{\mathrm{CCC}}[N_F - T_{L_1F}(s)N_1]. \tag{5}$$

It is assumed that the number of turns of the primary and feedback windings is fixed and has no uncertainty. AQ:4

The linkage current of the current comparator $1/G_{\mathrm{CCC}}$ was measured and found to be consistent with the data obtained three years earlier to within the measurement uncertainty (0.2%). Similar results were found for the flux sensitivity k_{SQ} but with 0.6% of uncertainty. In addition, the specification value of the SQUID cutoff frequency[1] was used [7]. AQ:5

The parameters in $T_{L_1F}(s)$ were measured or calculated individually. R_{W_1} was measured at 4.2 K using a high-accuracy

[1] At the SQUID design and assembly stage, this can be done by measuring the noise spectrum of the stand alone device, but this was not the case here.

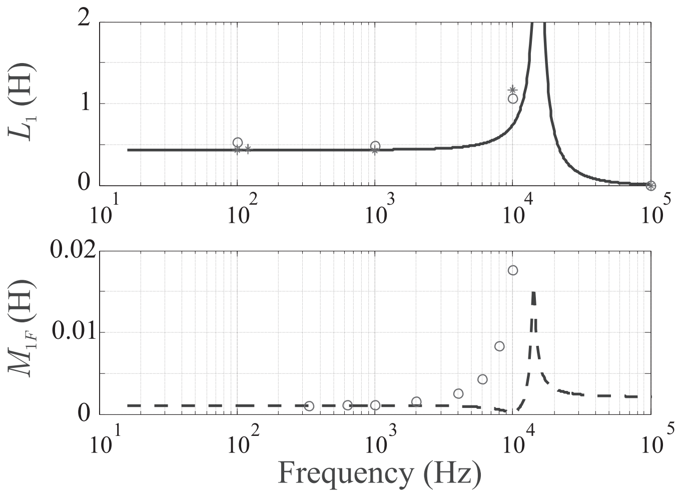

Fig. 3. Measurement results of L_1 and M_{1F}, in the top and bottom figures, respectively. The values at cryogenic (red star) and ambient (red circle) temperatures are shown. The simulations for the self-inductance at 4.2 K (blue solid line) and the mutual inductance at 300 K (blue dashed line) are also presented.

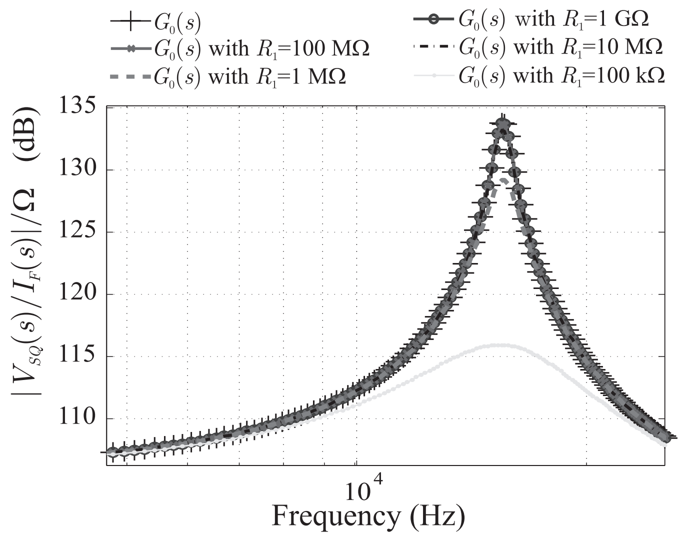

Fig. 4. Simulation of $G_0(s)$ (5) with six values of R_1. The transfer function for large value of resistance presents low deviations.

dc multimeter. Inductance L_1 was measured with an LCR meter, the resonant frequency was calculated as the average of many resonant peak observations and from these results, C_1 was obtained. The mutual inductance M_{1F} was determined by injecting a sinusoidal current in the feedback winding of one turn using a waveform generator and by measuring the voltage in the primary winding. The fast Fourier transform calculation of a digital oscilloscope was used to measure the amplitude of the desired frequency component. This measurement was performed at room temperature, and the self-inductance was also measured at 4.2 K (see Fig. 3). The resonant frequency of the coil with the greater number of turns (15.5 kHz) affects the measurements, for that reason, the values at lowest frequencies were used in the initial model. The inductance of the feedback winding, not shown in Fig. 3, presented a value of 2.6 μH at low frequencies. In addition, the effective self-inductance and mutual inductance were simulated. From (1) and (3), the effective value of these parameters was computed as $L_1 T_{L_1 1}(s)$ and $L_1 T_{L_1 F}(s) - M_{1F}$, respectively. In the case of the mutual inductance, the simulation was performed by setting the parameters to values obtained at room temperature.

Similarly, other important parameters can be simulated, e.g., the leakage current in the primary winding when $I_1(s)$ AQ:6 is injected can be calculated as $[1 - T_{L_1 1}(s)]I_1(s)$. Previous works have obtained similar results with models based on the electrical equivalent of the CCC [8], [9] or performing estimations assuming bridge balance and superconducting winding [10], [11]. The advantage of the Laplace representation is that it can be evaluated at different conditions, e.g., nonsinusoidal inputs. Furthermore, commercial programs are available to compute and improve the model [12].

To simplify the model identification, R_1 was set equal to 10 TΩ, therefore it was disconnected. Note that, (1)–(3) depend on R_1, and it attenuates the resonance of the primary winding. In Fig. 4, a simulation of the transfer function in (5) varying the resistance value of R_1 shows that the values larger than or equal to 10 MΩ generate negligible effects. On the other hand, a resistor of 1 MΩ or 100 kΩ connected to the primary winding strongly affects the transfer function. However, they are usually connected to windings with a low number of turns, producing a much lower attenuation. In this condition, the primary winding is in open circuit but the resonant frequency is damped due to the mutual inductance and stray capacitance arrangement of the CCC. These dynamics cannot be explained with (5). A complete model, that can include the effect of all the windings, resistors, and other associated dynamics, will lead to high-order equations and a more complicated controller. Therefore, a low-order model is desirable but in the following section, the model is expanded in order to include this behavior.

III. Model Set Identification

To improve the fitting of the theoretical model, a *grey-box* AQ:7 identification was performed using an iterative prediction-error minimization method [12]. It minimizes a cost function, defined as the weighted quadratic norm of the prediction error vector $v_{\mathrm{SQ}}(t) - \hat{v}_{\mathrm{SQ}}(t)$, at $t = t_q$. Here, $v_{\mathrm{SQ}}(t_q)$ is the experimental data and $\hat{v}_{\mathrm{SQ}}(t_q)$ is the estimated output at $t_q = q\ T_s$, $q \in \mathbb{Z}$ and T_s is the sampling period. The experimental frequency responses were measured with a lock-in amplifier [13]. The test current in the single turn feedback winding was generated using a voltage-to-current amplifier connected to the voltage source of the lock-in amplifier. A computer program was used to control the instrument in order to sweep the input frequencies. It also modifies the input amplitude at each step to avoid jumps or saturation of the SQUID. For a given configuration, the SQUID output and the input current were measured, the latter as a voltage drop in a high-quality metal film resistor connected in series. The magnitude of the transfer function was calculated as the ratio of the two measured values.

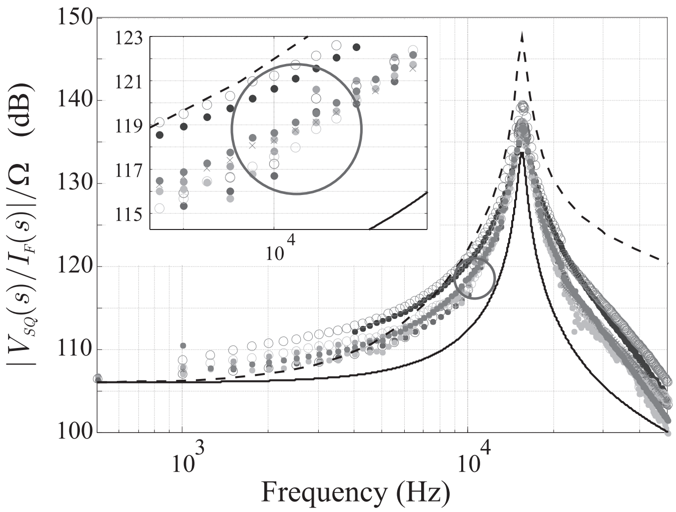

Fig. 5. Absolute value of the frequency response of the initial model (black dashed curve), identified model (black solid curve), and the experimental data measured with a lock-in amplifier. Different colored lines distinguish the different measurement days.

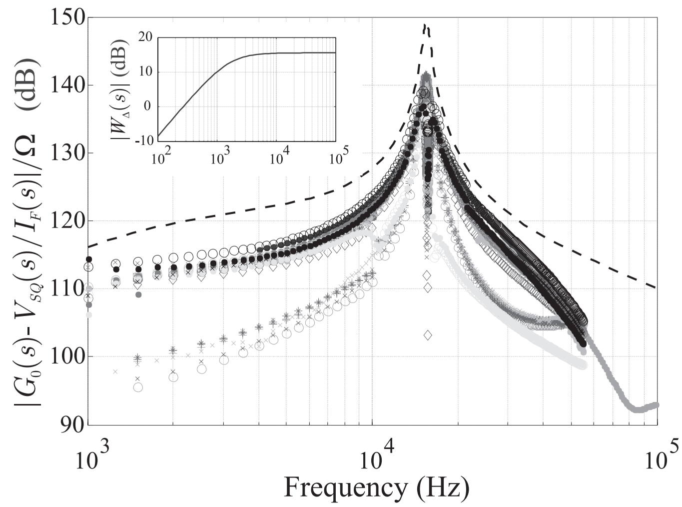

Fig. 6. Absolute value of the differences between the nominal model and the experimental data. The results are covered by the proposed dynamic uncertainty weight multiplied by the nominal model, $G_0(s) \cdot W_\Delta(s)$ (black dashed line). Inset: $W_\Delta(s)$.

TABLE I
INITIAL AND IDENTIFIED VALUES OF MODEL'S PARAMETERS

Parameter	Initial value	Identified value
K_{SQ}	0.779 V/Φ_0	Fixed
G_{CCC}	$(3.91\ \mu\text{AT}/\Phi_0)^{-1}$	Fixed
N_1	3100	Fixed
N_F	1	Fixed
R_{W1}	2850 Ω	Fixed
p	314 krad/s	314 krad/s
C_1	242 pF	242 pF
L_1	0.434 H	0.434 H
M_{1F}	**1.07 mH**	**0.22 mH**
R_1	10 TΩ	10 TΩ

Fig. 5 shows the initial and the identified models, and the experimental data. All the curves agree on the resonant frequency and the dc gain. Note that the experimental data are always above the identified model and in some curves, a small change can be found, which coincides with the modification of the excitation amplitude (see the inset of Fig. 5). This may be produced by noise at the SQUID output or an excursion of the SQUID working point. The input amplitude was selected to maximize the signal-to-noise ratio, to maintain the FLL ON, and to keep a low excursion of the working point.

In the optimization algorithm, some parameters were fixed because their off-line measurements showed a good repeatability and confidence. These values are summarized in Table I, together with the initial and identified values of other parameters. Only the mutual inductance was clearly affected by the identification algorithm adjustment.

Differences between the real and simulated frequency responses are generated by measurement errors and unmodeled dynamics [5], [14], [15]. Therefore, a more realistic description needs to include several models instead of a single one, in order to represent a physical system. Hence, in the robust control framework, the system is described as a model set with its center in the previously obtained nominal model. The set of models that fully describes the CCC dynamic behavior is defined as

$$\Psi = \{G(s) = G_0(s) \cdot [1 + W_\Delta(s) \cdot \Delta],\ \Delta \in \mathbb{C},\ |\Delta| \leq 1\}. \quad (6)$$

In this equation, $G(s)$ is a model included in the set, $G_0(s)$ is the identified nominal model, $W_\Delta(s)$ is the dynamic uncertainty weight, and Δ is an unknown complex number included in an unitary bounded set. At a given frequency $s = \jmath\omega$, all models included in the set belong to the circle of radius $|G_0(\jmath\omega) \cdot W_\Delta(\jmath\omega)|$ centered at $G_0(\jmath\omega)$. In this framework, $|W_\Delta(\jmath\omega)|$ represents the upper uncertainty bound of the model, as a function of frequency. If $|W_\Delta(\jmath\omega)|$ is larger than one at a frequency ω, the nominal model differs more than 100% from the real system, so a complete lack of knowledge of the system prevents control above that frequency [14], [15]. This is a practical result that indicates beforehand the maximum bandwidth that can be reached for this particular closed-loop controlled system.

To calculate the dynamic uncertainty weight, the nominal model was subtracted from the experimental data at each measured frequency and $W_\Delta(s)$ was adjusted to cover all these points. This is shown in Fig. 6, where the black dashed line is the proposed dynamic uncertainty weight multiplied by the nominal model $G_0(s) \cdot W_\Delta(s)$. The weight $W_\Delta(s)$ is shown in the inset of Fig. 6. It has a zero almost at the origin and a pole at $s = -10^4$, which produces a cutoff frequency of approximately 1.6 kHz. Note that above 300 Hz, $|W_\Delta(\jmath\omega)|$ is greater than unity (0 dB) and therefore limits the closed-loop bandwidth.

The experimental data were obtained by means of the lock-in amplifier and changing a setting and/or a parameter of the system, 33 frequency responses were evaluated. The purpose of these experiments was to represent different situations that may occur in practice and that should be covered by the model set Ψ. Time and liquid helium levels were the first variables to be analyzed. The measurements were performed during two weeks, while the He level varied between 43% and 10%

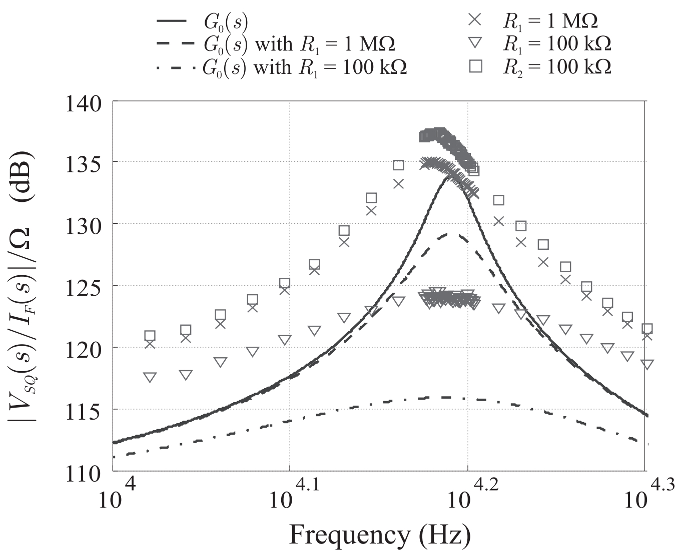

Fig. 7. Absolute value of the frequency response measurements (red) and simulation (blue) with a resistor connected. In the legend, the resistor and its position are indicated. The winding connected to R_1 has 10 times more turns than the winding in series to R_2.

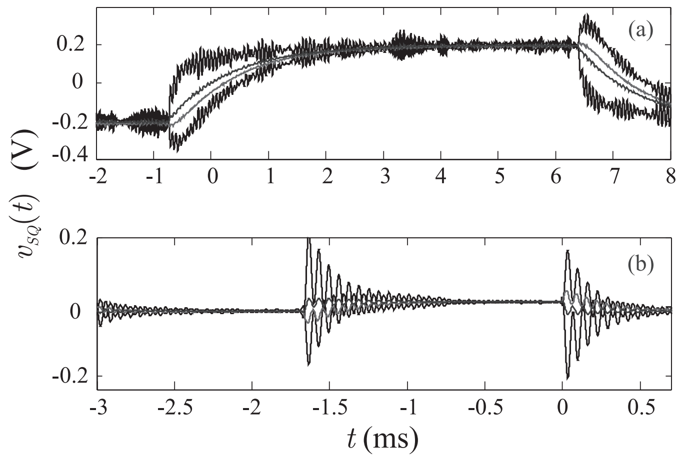

Fig. 8. Time response of the identified nominal model (blue line) and the experimental (red line) to a square wave input. Black lines represent the two extreme models of the set: 1) $G_{(\Delta=1)}$ and 2) $G_{(\Delta=-1)}$. The systems with $\Delta = \pm 1$ amplify more the high-frequency components in the recorder inputs, generating noisier outputs. Note that at 300 Hz, the uncertainty weight is equal to the nominal system (see the inset of Fig. 6) and the selection of Δ modified the gain of G. AQ:9

with one refill. The results do not show any dependence on these variables.

Other measurements were performed with 100 kΩ and 1 MΩ value resistors connected in parallel to one of the CCC ratio windings, to simulate real and extreme measurement configurations. As shown in Fig. 7, the resistor connected in parallel changes the resonant peak and frequency. However, the frequency shift is not explained by the theoretical model. Since the CCC probe is not designed to have a resistor connected in parallel to the winding, the circuit must be closed through the system ground. This can increase the parallel capacitance and decrease the resonant frequency. In fact, elements with these resistance values are usually connected to windings with a low number of turns. In these configurations, we found deviations of the measured frequency response from the nominal model within the repeatability of all the measured curves. Next, we extended the family of models to include uncommon and/or extreme settings in the set. To summarize, in the nominal model, primary resistor effects were neglected but they were included in the uncertainty weight. An alternative approach could be to make a model for each configuration; however, this was not possible on the system due to the extra capacitance problem, as it was explained at the beginning of this paragraph.

Finally, some measurements were performed with different
AQ:8 input windings as: 1) two 1-turn windings and 2) one 2-turns winding. No significant variations were found within the measurement repeatability. The feedback winding is not usually changed in real measurements; however, this experiment is useful to analyze the model. When the 2-turns feedback winding was used, the input current was multiplied by 2 in the calculations.

IV. Experimental Validation

The family of models was compared with the experimental data in order to evaluate the data fitting and coverage of the model set. Square, triangle, sinusoidal, and impulse waveform current signals were supplied to the feedback winding. A digital oscilloscope was used to measure and save the input signals and the SQUID output voltages synchronously. The responses of the nominal model were simulated and compared against the recorded outputs. An index that indicates the percentage of the output that the model reproduces [12] was calculated as

$$F_I = 100 \cdot \left(1 - \frac{|v_{\text{SQ}}(t) - \hat{v}_{\text{SQ}}(t_q)|}{|v_{\text{SQ}}(t) - \bar{v}_{\text{SQ}}|}\right), \quad \text{with} \quad t = t_q \quad (7)$$

where $\bar{v}_{\text{SQ}}$ is the mean value of $v_{\text{SQ}}(t)$. A perfect fit is represented with 100%, while 0% indicates that the model is equal to the mean value.

To this end, 34 measurements were performed with an average $F_I = 71\%$, two-third of these indexes were above this value. Two comparisons can be observed in Fig. 8 including the responses of two particular models in the set $G_{(\Delta=\pm1)} = G_0(s) \cdot [1 \pm W_\Delta(s)] \in \Psi$. From the first run [Fig. 8(a)], the nominal model output (blue line) was quite similar to the real one (red line) obtaining a fitting index better than 80%. This was not the case with the second simulation [Fig. 8(b)]. Note that the two extreme models (black lines) cover the actual output. These experiments confirm that a model (or models) exists within the set that fits the measured data. As a consequence, a controller that stabilizes the model set will also stabilize the actual physical system.

V. Closed-Loop Simulated Results

Based on the previous model set, an $\mathcal{H}_\infty$ optimal controller was designed in order to provide closed-loop stability and performance to all models in the set (and hence the physical system). Here, performance is quantified as the attenuation of noise and disturbances at the SQUID input, and it is measured by the $\mathcal{H}_\infty$ norm of the closed-loop transfer

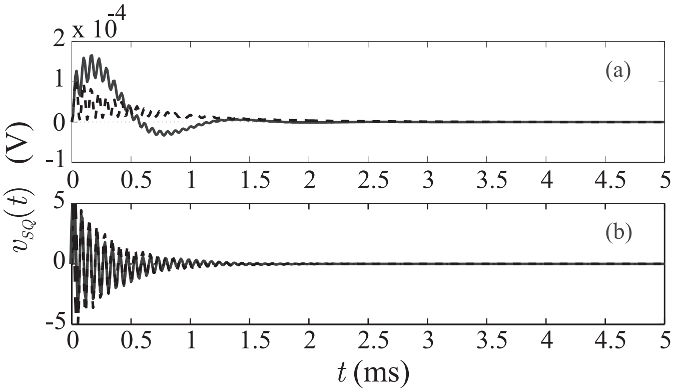

Fig. 9. (a) Step and (b) impulse simulated responses of the closed-loop system for the identified model (black dashed line) and the worst case model (blue solid line). The excitation amplitudes were 0.1 pA in the primary winding in both cases.

function. A mixed sensitivity procedure was applied, which balances the stability robustness and performance by means of uncertainty and performance weights [14]–[16]. The controller behaves as an integrator from dc to 1.6 kHz, and at the resonant frequency, its gain is sharply reduced and remained constant.

For a controller $K(s)$ connected to set Ψ, the set of all possible closed-loop transfer functions is as follows:

$$\mathcal{T} = \left\{ \frac{G_0(s)[1 + W_\Delta(s)\Delta]}{1 + G_0(s)[1 + W_\Delta(s)\Delta]K(s)}, |\Delta| < 1 \right\}. \quad (8)$$

The stability of the whole model set is guaranteed when the denominator of the previous equation does not vanish for all $G(s) \in \Psi$ and s is in the complex positive semiplane, i.e., $1 + G_0(s)[1 + W_\Delta(s)\Delta]K(s) \neq 0, \forall\ |\Delta| < 1,\ s \in \mathcal{C}^+$. It can be proved that a necessary and sufficient condition for controller $K(s)$ to stabilize all models in Ψ, defined as robust stability, is the following:

$$\left| \frac{G_0(s) \cdot K(s)}{1 + G_0(s) \cdot K(s)} W_\Delta(s) \right| < 1 \quad \forall\, s = \jmath\omega. \quad (9)$$

In this paper, this condition has been met. Fig. 9 shows this property, where the step and impulse responses of the nominal and worst case models [14]–[16] are represented, both being stable.

The performance of the $\mathcal{H}_\infty$ and the integrative controller can be compared with the closed-loop transfer functions. The $\mathcal{H}_\infty$ controller reduces the gain by 10 dB at the SQUID input up to 5 kHz. Since the design algorithm balances the robust stability and performance condition, the model uncertainty strongly affects the performance. Therefore, the uncertainty has to be considerably reduced. If the model uncertainty is minimized, the controller bandwidth can be increased until it attenuates the resonant peak without compromising the stability but this is difficult to achieve using traditional controllers.

VI. Conclusion

The CCC dynamic behavior was modeled by means of an identification procedure using the experimental data, an agreement of at least 70% was obtained. Thus, the electrical equivalent of the comparator seems to be a good approximation. Its parameters can be measured independently and/or computed from an identification process. A set of models were AQ:10 proposed to describe this system, and the simulations showed that all the recorded data were included. This strengthens the assumptions made in [5] to construct the model, especially those that neglect the stray capacitance of the windings (except for the one with the largest number of turns). An $\mathcal{H}_\infty$ controller was designed and robust stability for the model set was theoretically guaranteed and illustrated by the closed-loop simulations.

Here, the SQUID working point excursions and output noise floor limited the repeatability of the frequency response measurements. This fact increased the uncertainty and $|W_\Delta(\jmath\omega)|$, affecting the closed-loop performance. These two problems have opposite solutions, i.e., to reduce the noise effects a higher input signal is necessary, which can increment the working point excursion. A CCC with a lower resonant frequency and a larger SQUID bandwidth may accept a larger excitation input, increasing the signal-to-noise ratio. In this way, a smaller model uncertainty could be obtained and a faster controller could be designed.

Acknowledgment

The authors would like to thank M. Götz from PTB-Germany and M. Cazabat from INTI-Argentina for many AQ:11 valuable discussions.

References

[1] J. M. Williams, "Cryogenic current comparators and their application to electrical metrology," *IET Sci. Meas. Technol.*, vol. 5, no. 6, pp. 211–224, Nov. 2011.

[2] D. Drung, M. Götz, E. Pesel, J.-H. Storm, C. Aßmann, M. Peters, and T. Schurig, "Improving the stability of cryogenic current comparator setups," *Supercond. Sci. Technol.*, vol. 22, no. 11, p. 114004, 2009.

[3] K. Jones and M. D. Early, "A quantum Hall cryogenic current comparator resistance bridge," in *CPEM Dig.*, Sydney, NSW, Australia, May 2000, pp. 92–93.

[4] F. L. Hernandez-Marquez, M. E. Bierzychudek, G. R. Jones, Jr., and R. E. Elmquist, "Precision high-value resistance scaling with a two-terminal cryogenic current comparator," *Rev. Sci. Instrum.*, vol. 85, no. 4, p. 044701, 2014.

[5] M. E. Bierzychudek, R. S. Sánchez-Peña, and A. Tonina, "Robust control of a two-terminal cryogenic current comparator," *IEEE Trans. Instrum. Meas.*, vol. 62, no. 6, pp. 1736–1742, Jun. 2013.

[6] R. E. Elmquist, E. Hourdakis, D. G. Jarrett, and N. M. Zimmerman, "Direct resistance comparisons from the QHR to 100 MΩ using a cryogenic current comparator," *IEEE Trans. Instrum. Meas.*, vol. 54, no. 2, pp. 525–528, Apr. 2005.

[7] Quantum Design. *DC + RF SQUID Systems Brochure*. [Online]. Available: http://www.qdusa.com/sitedocs/productBrochures/squid3.pdf

[8] F. Rengnez, O. Séron, L. Devoille, D. Placko, and F. Piquemal, "A femto ampere current amplifier based on a 30 000:1 cryogenic current comparator," in *CPEM Dig.*, Rio de Janeiro, Brazil, Aug. 2014, pp. 296–297.

[9] K. Grohmann and D. Hechtfischer, "Self-calibrating cryo current comparators for AC applications," *IEEE Trans. Instrum. Meas.*, vol. 33, no. 2, pp. 91–96, Jun. 1984.

[10] F. Delahaye, "An AC-bridge for low-frequency measurements of the quantized Hall resistance," *IEEE Trans. Instrum. Meas.*, vol. 40, no. 6, pp. 883–888, Dec. 1991.

[11] H. Seppä and A. Satrapinski, "AC resistance bridge based on the cryogenic current comparator," *IEEE Trans. Instrum. Meas.*, vol. 46, no. 2, pp. 463–466, Apr. 1997.

[12] L. Ljung, *System Identification Toolbox—User's Guide*, 9th ed. Natick, MA, USA: MathWorks, Mar. 2014.

[13] T. B. Lawson, M. D. Early, and K. Jones, "Simulation of a quantum Hall cryogenic current comparator resistance bridge," in *CPEM Dig.*, Daejeon, Korea, Jun. 2010, pp. 623–624.

[14] K. Zhou, J. C. Doyle, and K. Glover, *Robust and Optimization Control*. AQ:12 Englewood Cliffs, NJ, USA: Prentice-Hall, 1996.

[15] R. S. Sánchez-Peña and M. Sznaier, *Robust Systems Theory and Applications*, 1st ed. New York, NY, USA: Wiley, 1998.

[16] G. J. Balas, J. C. Doyle, K. Glover, A. Packard, and R. Smith, *μ-Analysis and Synthesis Toolbox—User's Guide*, 3rd ed. Natick, MA, USA: MathWorks, Jun. 2001.

Marcos Eduardo Bierzychudek received the Electronics Engineering degree from the Universidad de Buenos Aires, Buenos Aires, Argentina, in 2006.

He joined the Electricity Division, Instituto Nacional de Tecnología Industrial, Buenos Aires, in 2005. He has been with the Quantum Electrical Metrology Laboratory, where he is involved in measurements of the Josephson effect and the Quantum Hall effect.

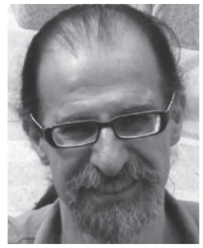

Ricardo S. Sánchez-Peña (S'86–M'88–SM'00) received the Electronic Engineering degree from the Universidad de Buenos Aires (UBA), Buenos Aires, Argentina, in 1978, and the M.Sc. and Ph.D. degrees in electrical engineering from the California Institute of Technology, Pasadena, CA, USA, in 1986 and 1988, respectively.

He was with CITEFA, CNEA, and the space AQ:13 agencies CNIE and CONAE from 1977 to 2004. He collaborated with NASA, the German (DLR), and Brazilian (CTA/INPE) space agencies. He was a Full Professor with UBA from 1989 to 2004, an ICREA Senior Researcher with the Polytechnic University of Catalonia, Barcelona, Spain, from 2005 to 2009, and a Visiting Professor/Researcher with several universities in the USA and the EU. He has consulted for ZonaTech, Scottsdale, AZ, USA, Alstom-Ecotecnia, Barcelona, Spain, STI, Buenos Aires, and VENG, Buenos Aires. Since 2009, he has been the Director of the Ph.D. Department with the Instituto Tecnológico de Buenos Aires, Buenos Aires, and a CONICET Principal Investigator. He has applied identification and control techniques to practical problems in engineering and medicine. He has authored three books and over 140 journal and conference papers.

Alejandra Tonina was born in Buenos Aires, Argentina. She received the Licenciatura and Ph.D. degrees in physics from the University of Buenos Aires, Buenos Aires.

She joined the Instituto Nacional de Tecnología Industrial, Buenos Aires, in 1998. Her main responsibility is related to the maintenance of the electrical quantum standards. She is involved in research on QHE and new measurement techniques of the electrical magnitudes.